THE ACCOMMODATION COEFFICIENT OF SALINE SESSILE WATER DROPLETS EVAPORATING WITH VARYING NON-VOLATILE IMPURITY LOADS

Murray B. and Narayanan S.*
*Author for correspondence
Department of Mechanical, Aerospace, and Nuclear Engineering,
Rensselaer Polytechnic Institute,
Troy, NY 12180, USA.
E-mail: narays5@rpi.edu

ABSTRACT

Air-water evaporation systems are ubiquitous in industrial applications, including processes such as fuel combustion, inkjet printing, spray cooling, and desalination. In these evaporation-driven systems, a fundamental understanding of mass accommodation at the liquid-vapour interface is critical to predicting and optimizing performance. Interfacial mass accommodation depends on many factors, such as temperature, vapour concentration, non-volatile impurity content, and non-condensable gasses present. Elucidating how these factors interact is essential to designing devices to meet demanding applications. Hence, high precision measurements are needed to quantify accommodation at the liquid-vapour interface accurately. Our previous study has shown surface averaged accommodation coefficients close to 0.001 for pure water droplets throughout evaporation. While it is well established that saline non-volatile impurities reduce the evaporation rate of sessile droplets, the dynamic effect on mass accommodation during the droplet's lifespan is yet to be determined. In this work, we combine experimental and computational techniques to determine the accommodation coefficient over the lifespan of 10^{-3} to 1 molar potassium chloride-water droplets evaporating on a gold-coated surface into dry nitrogen. This study uses a quartz crystal microbalance as a high-precision contact area sensor. It also determines the non-volatile impurities in the droplet with a precision on the order of nanograms. The computational model couples macroscopic measurements with the microscopic kinetic theory of gasses to quantify hard-to-measure physical quantities. We believe this study will provide a basis for predicting evaporative device performance in conditions where non-volatile impurities are intrinsic to the application.

INTRODUCTION

Evaporation of sessile droplets has seen an extensive study in recent years to leverage evaporation kinetics, control heat transfer and deposit solid particles [1]. Specifically, evaporation of aqueous solutions is essential for DNA mapping, diagnosis of diseases [2], spray cooling [3], corrosion [4], desalination [5], microelectronic cooling, inkjet printing, and power apparatus applications [6]. Droplets of saline solutions can be challenging to study, with salt concentration increasing over time as the water in the droplet evaporates, leading to non-linear evaporation rates, heat fluxes, and crystallization phenomena [7].

NOMENCLATURE

c	[mol/m^3]	Molar vapour concentration
C_p	[J/kg/K]	Specific heat capacity at constant pressure
D	[m^2/s]	Diffusion coefficient
f	[Hz]	Resonant frequency
$\boldsymbol{I}$	[-]	Identity matrix
J	[mol/m^2/K]	Molar flux
k	[W/m/K]	Thermal conductivity
L_{vap}	[J/mol]	Molar latent heat of vaporization
M	[kg/mol]	Molar mass
m	[mol/kg]	Molality of solution
$\boldsymbol{n}$	[-]	Normal vector away from droplet surface
p	[Pa]	Total pressure
$\boldsymbol{q}$	[W/m^2]	Heat flux vector
R	[mol/J/K]	Universal gas constant
r	[m]	Radius
T	[K]	Temperature
$\boldsymbol{u}$	[m/s]	Velocity vector
V	[m^3]	Droplet volume

Greek Symbols

θ	[rad]	Droplet contact angle
λ	[mol/m^3]	Lagrange multiplier
μ	[Pa*s]	Viscosity
ρ	[kg/m^3]	Density
σ	[-]	Accommodation coefficient
χ	[-]	Mole fraction

Superscripts

N	Nitrogen gas component
W	Water vapour component

Subscripts

d	Of the droplet
e	Of the QCM electrode
g	Of the gaseous vapour
iv	At the vapour side of the liquid-vapour interface
l	At liquid side of liquid-vapour interface
s	Saturation value
v	Evaluated at the end of the Knudsen layer

Liquid water is notoriously hard to keep pure and tends to accumulate impurities. Typically, water contains surfactants, electrolytes, and dissolved gasses as impurities in many applications. A large body of work focuses on the simpler case of pure water evaporating into an atmosphere of water vapour and non-condensable gas mixture. Even in this far less complex case, much debate surrounds the nature of interfacial mass accommodation at the liquid-vapour interface during evaporation. The mass accommodation coefficient (AC) in

Schrage's relationship (Eq. (1)) derived from the kinetic theory of gasses has been reported to vary over three orders of magnitude from 10^{-3} to 1 for evaporating water [8,9]. This variation could be due to various definitions of ACs, dissimilar experimental conditions, and dissolved impurities. Furthermore, considering AC as a material property that depends on the liquid-vapour interface state, measuring the quantities needed to characterize the AC can be a challenge since pressure and temperature can vary across the Knudsen layer, which is on the order of the mean free path of a vapour molecule (~86 nm for water at 1 atm). Consequently, prior reports show significant disagreement in the temperature change across the Knudsen layer, with some cases also requiring extrapolation of data [10], which could have also resulted in significantly different ACs.

Our previous work coupling high-precision experimental measurements with multiscale computational modelling to investigate droplet evaporation into dry nitrogen flow indicates AC values close to 10^{-3} for nominally pure water at atmospheric conditions. While the exact form of relationships between interfacial mass accommodation and factors such as temperature, vapour concentration, non-volatile impurities, and non-condensable gasses are not known explicitly, some trends are clear. For example, increasing non-condensable gas pressure and the accumulation of non-volatile impurities are both known to decrease AC to some extent [9].

This study focuses on elucidating the effect of dissolved non-volatile impurities (potassium chloride, KCl) on mass accommodation at the liquid-vapour interface by utilizing a multi-scale computational and experimental framework. We believe that the AC's determined using droplets with controlled impurity can serve as a predictive tool in designing systems involving saline water evaporation.

BACKGROUND THEORY

This work focuses on a liquid evaporating into a mixture of its own vapour and a non-condensable gas (nitrogen). By accounting for each component, the equations for the molar flux for the evaporating liquid are given by [8]:

$$J^i = \sigma^i \sqrt{\frac{R}{2\pi M^i}} \left(c_s^i(T_l)\sqrt{T_l} - c_v^i \sqrt{T_v}\Gamma(\phi_v^i) \right) \quad (1)$$

$$\Gamma(\phi_v^i) = e^{-{\phi_v^i}^2} - \phi_v^i \sqrt{\pi}(1 - \mathrm{erf}(\phi_v^i)) \quad (2)$$

$$\phi_v^i = \sqrt{\frac{2RT_v}{M^i}} \sum_i \frac{J^i}{c_v^i} \quad (3)$$

Expanding Eq. (1) into two equations, one for each component (superscript i) and with $J^N(\text{nitrogen flux}) \approx 0$ gives Eq. (4) for the flux of water and Eq. (5) for the temperature and pressure change across the Knudsen layer.

$$J^W = \sigma^W \sqrt{\frac{R}{2\pi M^i}} \left(c_s^W(T_l)\sqrt{T_l} - c_v^W \sqrt{T_v}\Gamma(\phi_v^W) \right) \quad (4)$$

$$c_{iv}^N \sqrt{T_l} = c_v^N \sqrt{T_v}\Gamma(\phi_v^N) \quad (5)$$

Eq. (5) can then be written in terms of water vapour properties by taking the two-component mixture to behave like an ideal gas ($p = cRT$) and the partial pressures of each component adding to the total pressure on each side of the Knudsen layer to result in Eq. (6).

$$\sqrt{\frac{T_v}{T_l}} = \frac{p_v - c_v^W RT_v}{p_{iv} - c_s^W(T_l)RT_l}\Gamma(\phi_v^N) \quad (6)$$

From Eq. (6), the temperature jump $(T_l - T_v)$ is related to both the pressure change $(p_{iv} - p_v)$ and concentration change $(c_s^W - c_v^W)$ over the Knudsen layer. With absolute pressure of 10^5 Pa, the ratio p_{iv}/p_v is nearly unity, we take the pressure to be constant across the Knudsen layer to calculate the temperature jump based on the concentration change over the Knudsen layer.

EXPERIMENTAL PROCEDURE

Precise techniques are needed to monitor the droplet geometry during evaporation to study mass accommodation during evaporation. Here a quartz crystal microbalance (QCM) is used as a high-precision contact area sensor. Typically used to monitor deposition processes because of the linear relationship between frequency change and a rigid mass, as described by the Sauerbrey equation [11], these sensors can also accurately monitor sessile droplet contact area [12,13].

The resonant frequency of a QCM can be monitored to deduce changes in phenomena occurring on the surface, such as rigid mass deposited on the surface, changes in liquid density, viscosity, and contact area. An equation validated for use with droplets was derived based on the shear stress developed between the oscillating QCM surface and a liquid droplet in Ref. [12] and is shown below in Eq. (7).

$$\Delta f = f - f_0 = -f_0^{\frac{3}{2}} \frac{\sqrt{\rho_d \mu_d}}{Z_q \sqrt{\pi}} \left(1 - e^{-2a\frac{r_d^2}{r_e^2}} \right) \quad (7)$$

Here, the droplet contact radius (r_d) can be related to a measured frequency shift (Δf) relative to the initial frequency (f_0) in terms of known liquid and quartz parameters where $Z_q = 8.84 \times 10^6$ kg/m^2/s. In this work, a 10 MHz AT-cut QCM with gold keyhole-shaped electrodes is used (Figure 1(a)), and sensitivity parameter a is taken to be unity as in previous works [12,13]. During evaporation, the frequency recorded over time gives the droplet radius from start to finish.

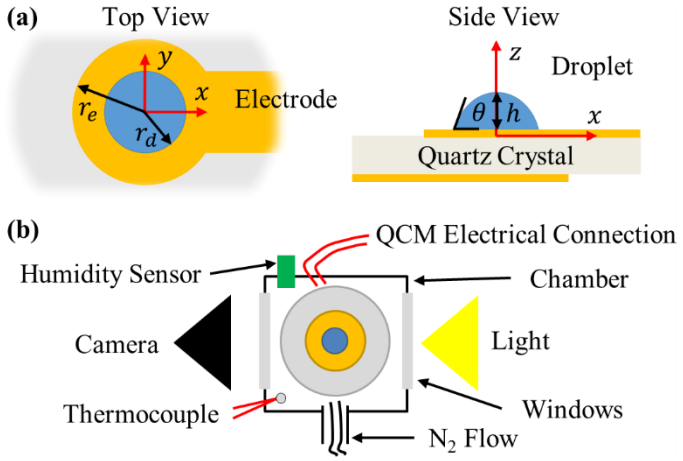

Figure 1 (a) Top and side view of planar AT-cut QCM with keyhole-shaped electrodes loaded with a centrally placed sessile droplet. (b) Top view of experimental enclosure, with labelled components

The QCM response to millimetre-sized droplets is insensitive to changes in contact angle, and additional information is needed to determine the volume of the droplets. A goniometer (ramé-hart 590-U2) was used to determine the contact angle of the

sessile droplets so that the contact angle and radius data can be used in Eq. (8) to determine the volume of the droplet over time.

$$V = \frac{\pi}{6} r_d^3 \tan\left(\frac{\theta}{2}\right)\left(3 + \tan^2\left(\frac{\theta}{2}\right)\right) \quad (8)$$

A piecewise weighted least-squares linear fitting of overlapping segments was used to determine the volumetric evaporation rate [13,14]. This approach found a best fit line to the volume data in 80 s intervals that were centred 40 s apart, and the relative uncertainty in the volume (propagated from uncertainty in contact angle and frequency measurements) was used as a weight to determine the uncertainty in the slope of the best fit lines. The slope provides the average volumetric evaporation rate over the corresponding time interval.

Before each experiment, the QCM was cleaned with a series of sonication steps in solutions of 50 mM NaOH, 1:2 toluene to acetone, acetone, isopropyl alcohol, and de-ionized (DI) water. The QCM was suspended in each of these solutions for at least 5 minutes and finally dried in pure nitrogen.

Experiments were conducted inside of a 45 x 45 x 299 mm aluminium enclosure (Figure 1(b)) that was maintained at room temperature and was supplied nitrogen gas at low speed (70-95 L/hr), measured by a rotameter with uncertainty ±5 L/hr. The nitrogen flow displaced moisture resulting in a constant humidity of <5% in the enclosure. Humidity and temperature measurements were performed by a Honeywell HIH-4000 and J-type thermocouples (±0.5 K uncertainty), respectively. Experiments used DI water with evaporation residue < 1 ppm (HiPerSolv, VWR) and as received potassium chloride (KCl) (Fisher Chemical, >99.4%) to create solutions of 0-1 molar (0-1.03 molal). Droplets were deposited onto the QCM with a manual syringe that entered the enclosure through a 3.2 mm diameter hole directly above the centre of the QCM (not shown in Figure 1(b)). Frequency was recorded using an eQCM system (Gamry Instruments).

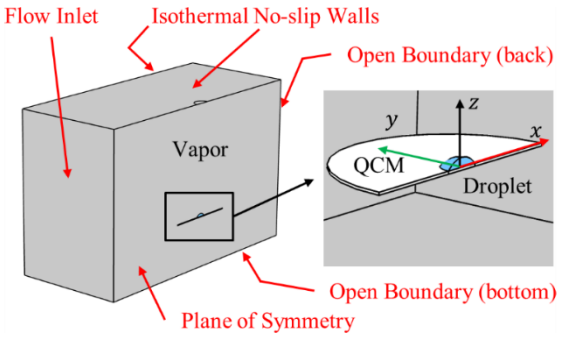

Figure 2 The entire computational domain is shown on the left with exterior boundary conditions (red text). A close-up of the QCM and water droplet are shown on the right with the Cartesian axis directions labelled. The origin is located at the centre of the base of the droplet

COMPUTATIONAL METHOD

A computational model was developed to couple the macro-scale experimental measurements with the kinetic theory of gasses, which provides interfacial conditions to determine the extent of mass accommodation at the liquid-vapour interface. Due to the low evaporation rates found in this work, droplet evaporation can be assumed quasi-steady, meaning the vapour distribution and flow patterns adjust to changes in droplet geometry much faster than the change in the droplet shape. Hence, the model neglects contact line dynamics to focus on the interface at a given time and droplet geometry (radius and contact angle).

A representative domain (Figure 2) is created employing the symmetry found in the experimental work. Figure 2 shows the water droplet's position on a flat quartz substrate surrounded by a gaseous domain that contains nitrogen and water vapour. The model is solved in commercially available finite element software, COMSOL Multiphysics® [15]. The model uses a range of element shapes to mesh the complex geometry, with a total of > 800,000 elements and > 1,200,000 degrees of freedom.

The governing equations of this model are Fourier's law (Eq. (9)), conservation of energy (Eq. (10)), and compressible Navier-Stokes (Eq. (11)), conservation of mass (Eq. (12)) as well as convective and diffusive transport of water vapour (Eq. (13)). In the liquid domain, the temperature and velocity gradients are small and not large enough to affect the evaporation rate for water droplets of this size [16]. Therefore, $\boldsymbol{u} \approx 0$ in the liquid domain. Additionally, the flow is not significantly affected by buoyancy in the droplet's vicinity because of the imposed cross-flow and the low-density gradients so that that gravity can be neglected in Eq. (11).

$$\boldsymbol{q} = -k\nabla T \quad (9)$$

$$\rho C_p \boldsymbol{u} \cdot \nabla T + \nabla \boldsymbol{q} = 0 \quad (10)$$

$$\rho_g (\boldsymbol{u} \cdot \nabla)\boldsymbol{u} = \nabla \cdot \left[-p\boldsymbol{I} + \mu_g(\nabla \boldsymbol{u} + (\nabla \boldsymbol{u})^t)\right] \quad (11)$$

$$\nabla \cdot \left(\rho_g \boldsymbol{u}\right) = 0 \quad (12)$$

$$\nabla \cdot (-D\nabla c^W + \boldsymbol{u} c^W) = 0 \quad (13)$$

The model does not explicitly solve the Knudsen layer but employs equations (Eqs. (4) & (6)) to calculate the change in properties (water vapour concentration, temperature) over the Knudsen layer.

The boundary conditions on the top and left exterior boundaries of the domain are taken as non-slip walls at constant temperature (from experimental measurement). The downstream and bottom boundaries are 'open boundaries' where there is no condition imposed on the impinging flow, but any flow into the domain is treated as $c^W = 0$ at the experimentally measured enclosure temperature. The boundary on the right is a symmetry plane, with no flow or flux allowed through it. The inlet condition for temperature and water vapour concentration is an 'open boundary,' while the velocity condition is a prescribed flow field. By solving a model of the entire enclosure's flow, it was found that the flow 25.4 mm upstream of the droplet is steady throughout evaporation and across experiments. Hence, this velocity profile can be directly imposed at this location upstream of the droplet to reduce computational costs significantly compared to solving the entire enclosure's flow for every data point of interest. The external boundary conditions can be seen graphically in Figure 2.

At the liquid-vapour interface, the evaporative self-cooling can be implemented as a heat sink on the liquid side of the interface, $-\boldsymbol{n} \cdot \boldsymbol{q} = -L_{vap} J$. Instead of solving the Knudsen layer directly, Eqs. (4) & (6) can be used to calculate the differences in temperature and concentration from the liquid-vapour interface to the bulk vapour. These variations in

temperature and concentration can be seen schematically in Figure 3. Eq. (6) is expanded to a three-term Maclaurin series and simplified with $\Gamma(\phi_v^N) \approx 1$ and $p_{iv} = p_v = p$, to obtain Eq. (14) which makes implementing a temperature discontinuity in the model possible. This expansion is accurate to the sixth significant digit for T_v under these experimental conditions.

$$T_v \approx T_l + \frac{R}{p}(c_s^W - c_v^W)\left(2T_l^2 + \frac{R}{p}(3c_s^W - 5c_v^W)T_l^3\right) \quad (14)$$

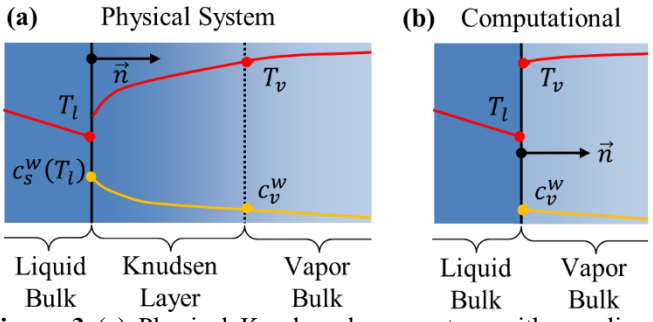

Figure 3 (a) Physical Knudsen layer system with non-linear variation of temperature and concentration. (b) Computational implementation of the physical system with a jump in properties supplied in place of the Knudsen layer

Finally, the vapour concentration at the Knudsen layer's edge is solved using a Lagrange multiplier approach to obtain the same flux as measured experimentally. The flux at the end of the Knudsen layer into the bulk gaseous vapour is defined locally as $\boldsymbol{J} = -D\nabla c^W$. The total molar flux of the droplet is prescribed by an integral constraint based on the experimental volumetric evaporation rate,

$$-\dot{V} = M^W \iint \frac{1}{\rho_l}\boldsymbol{n}\cdot\boldsymbol{J}dA \quad (15)$$

To enforce this constraint, the concentration at the edge of the Knudsen layer need not be identical to the saturation concentration at the liquid-vapour interface. Therefore, the water vapour concentration is determined as $c_v^W = c_s^W(T_l) - \lambda$. Physically the Lagrange multiplier can be thought of as the concentration change over the Knudsen layer.

The saturation concentration of the droplet depends on the salt content. The lowering of the saturation concentration can be calculated by Raoult's law, $c_s^W(T_l) = \chi^W c_{s_{pure}}^W(T_l)$. Here the water mole fraction is defined as in Zavitsas [17] with $H_d = 2.1$ and $i_e = 1.75$ for KCl, $\chi^W = (55.509 - m\,H_d)/(55.509 - m\,H_d + m\,i_e)$. The initial water mole fraction for droplets of 0, 0.001, 0.1, and 1 M KCl solution are 1, 0.999968, 0.9968, and 0.9672, respectively.

In this work, we consider only the initial stages of evaporation where the molality in each droplet has not significantly changed. Hence, we assume evenly dispersed potassium and chloride ions in the droplet during the initial stage and that the interface has the same molality as the bulk droplet. After sufficient evaporation, the accumulation of salt at the liquid-vapour interface cannot be ignored. In this case, the local (interfacial) KCl concentration would determine the appropriate saturation concentration via Raoult's law.

Most material properties required for the model were obtained from Ref. [18], with quartz heat capacity from Ref. [19], aqueous electrolytic solution properties of thermal conductivity, density, viscosity, and heat capacity from Refs. [20,21]. Temperature dependence is included for all liquid and gaseous properties. Additionally, the density of the gaseous vapour is modified by the presence of lighter water vapour, $\rho_g = \rho_{dry}^N + c^W(M^W - M^N)$.

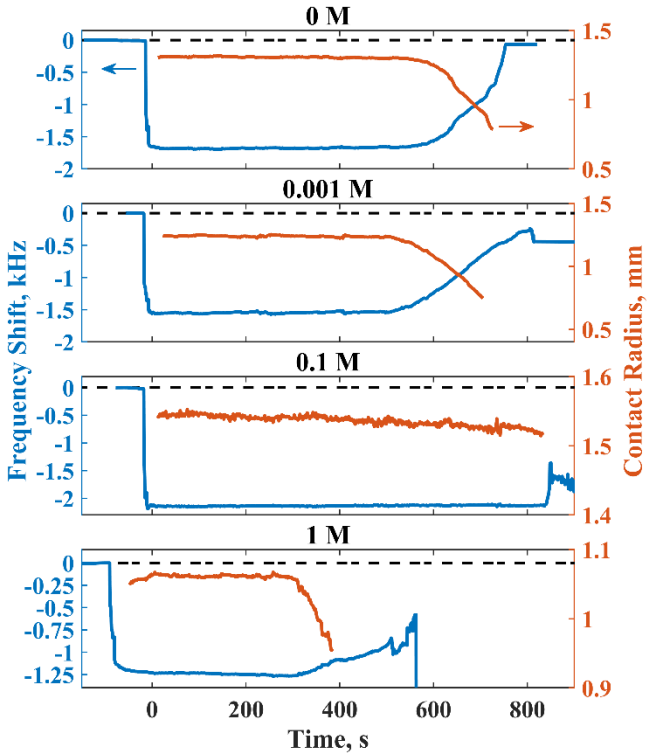

Figure 4 Frequency response (left axis) and droplet contact radius (right axis) over time for droplets of various KCl concentrations. Droplet contact radius was calculated from the frequency response data taking $a = 1$ and $r_e = 2.58$ mm with Eq. (7)

RESULTS AND DISCUSSION

We performed multiple experimental trials of sessile droplet evaporation with water droplets containing 0, 0.001, 0.1, and 1 M solutions of KCl. Frequency data from these four trials can be seen in Figure 4. Here, an initial plateau before droplet deposition is seen, followed by deposition of the droplet and then a steady frequency response corresponding to a constant contact radius mode of evaporation. In the 1 M trial, the frequency is slowly decreasing during the constant contact radius mode. However, this phenomenon is not due to the spreading of the droplet. Instead, this decrease in frequency can be explained by an increase in the density-viscosity product ($\rho_d\mu_d$) in Eq. (7) due to the increasing KCl concentration. When Eq. (7) is employed to determine the droplet contact radius, this effect is accounted for in the fluid properties. After some time in each trial, the frequency begins to increase, corresponding to a decrease in the contact radius with the droplets entering a variable contact radius mode of evaporation. In the case of the pure water (0 M) trial, the frequency increases back to nearly the

same value ($\Delta f \approx 0$ Hz) at the end of evaporation. For the droplets containing KCl, this is not the case. The frequency response corresponding to the highly complex deposition process at the end of evaporation is challenging to analyse. The dual effects of droplet drying (density, viscosity, area changes) and non-uniform deposition of KCl onto the QCM surface cause a frequency response that is not easily distinguishable. However, qualitatively, the higher concentrations of salt causes more significant frequency shifts at the end of evaporation due to larger amounts of mass being deposited on the crystal. For the 1 M droplet, the final frequency shift is approximately -6 kHz and is not shown in Figure 4 for clarity.

Employing Eq. (7), the radius can be determined for each droplet, and in combination with the contact angle measurements, the volume can be determined. Figure 5(a) shows the volume of each trial over time. While no apparent trend in evaporation rate is clear from this data due to slightly differing initial volumes and droplet geometries, the 1 M trial can be seen to have the shallowest slope of the four experimental trials. This shallow slope corresponds to the lowest evaporation rate of the four trials.

Figure 5(b) shows the evaporation rate of each trial. If the droplets were of the same geometry, the evaporation rate would be expected to be ordered by the salt content (lowering vapour pressure). However, droplet evaporation rate is also dependent on geometry (radius, contact angle) [1]. The cause of the slight geometry variation in this work is due to changes in surface tension from the addition of KCl and variations in the manual deposition process. This variation in size does not affect the study's goal of determining the AC of various aqueous solutions. Although, it can make comparing the evaporation rate of droplets challenging. There is an overall decreasing trend in each droplet's evaporation rate that can be attributed to a combination of an increased proportion of non-volatile impurities and decreasing contact angle and radius. The evaporation rate of a pure fluid isothermal droplet is expected to scale with the contact radius $\left(\dot{V} \propto r_d\right)$ in a purely diffusive environment and scales with the surface area in an advectively driven case $\left(\dot{V} \propto r_d^2\right)$ [1]. Hence, with a low-speed dry nitrogen flow around the droplet, the evaporation is of mixed diffusive-advective character; neither scaling law is entirely appropriate.

The volumetric evaporation flux (Figure 5(c)), defined as the ratio of the evaporation rate to the surface area $\left(\dot{V}'' = \dot{V}/2\pi r_d^2(1+\tan(\theta/2)\right)$, does not show a decreasing trend. Rather, the evaporation flux for each droplet is approximately constant until the final few data points. The tendency to increase seen in these final data points of Figure 5(c) is due to the decreasing radius, providing an increased $\dot{V}''$. This is not seen in the 0.1 M trial because it has a near constant radius during its lifetime. Additionally, the peak in the 0.001 M evaporation rate at ~450 s is due to background lighting and reflection disturbing the contact angle and volume measurements, which affected the linear slope determination.

The trend of AC with increasing KCl concentration is expected to be downward. However, in Eq. (4), both the left-hand side (J^W) and right-most term on the right-hand side $\left(c_s^W(T_l)\sqrt{T_l} - c_v^W\sqrt{T_v}\Gamma(\phi_v^W)\right)$ decrease with increasing KCl concentration. The decrease in J^W can be seen in Figure 5(c), while the decrease in the latter term can be inferred from the decrease in $c_s^W(T_l)$ via Raoult's law and the similar experimental temperatures of all the experiments (23.5-26.5 °C) holding the other values relatively constant. Thus, for the AC to decrease with increasing KCl concentration, the left-hand side must decrease relatively more than the latter term on the right-hand side.

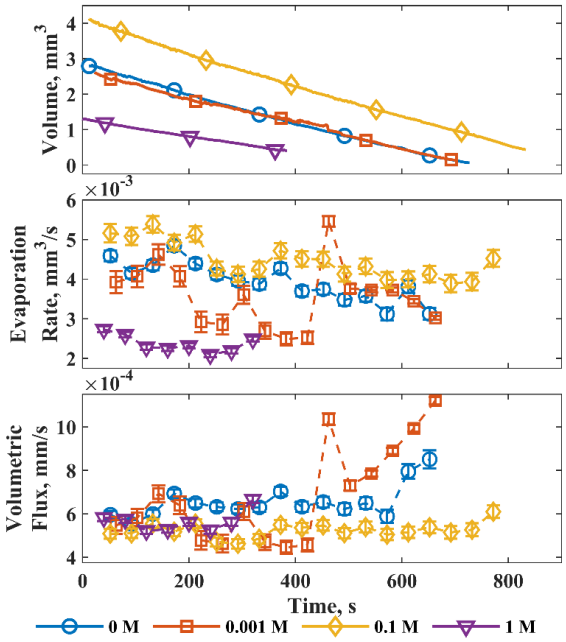

Figure 5 (a) Volume calculated from Eq. (8) for various experiments. (b) Evaporation rate determined by a weighted least-squares regression over 80-second intervals of volume data. (c) Volumetric flux calculated as evaporation rate divided by surface area for droplets with various KCl concentration

The AC corresponding to each KCl concentration is shown in Figure 6. The AC was calculated using the first three evaporation rate data points as individual inputs to the computational model to obtain three surface-averaged ACs and their associated uncertainties. To obtain the surface-averaged AC, the local AC is first computed using Eq. (4) across the entire droplet surface using local properties (molar flux, temperature, vapour concentration, pressure) and then averaged over the surface of the droplet. The model calculates the sensitivity of the main input parameters (evaporation rate, temperature, and nitrogen gas flow rate), and this is used to determine the uncertainty of the calculated AC value. For each concentration of KCl, the three ACs of the first three times are combined into a mean AC $(\bar{\sigma})$ by means of a weighted average where the weights are the inverse square of the uncertainty (δ_i) of each of the individual ACs (σ_i), $\bar{\sigma} = \sum \delta_i^{-2}\sigma_i / \sum \delta_i^{-2}$. The uncertainty of the mean AC $\left(\bar{\delta}\right)$ can also be found, $\bar{\delta} = 1/\sqrt{\sum \delta_i^{-2}}$.

The mean AC is shown in Figure 6 with error bars as $\bar{\sigma} \pm \bar{\delta}$. The droplet without KCL has the highest averaged AC, where the 1 M concentration has the lowest. This outcome in and of itself is not surprising. However, what is notable here is the

amount of decrease from the 0 M droplet to the 1 M droplet - a factor of two, where the saturation pressure only reduces by ~3%. Additionally, Figure 6 shows a continual decrease from 0 to 1 M KCl. Lower than 0.001 M KCl, the AC is expected to asymptote to the value at nominally pure water in an atmosphere consisting of majority non-condensable gas (~ 0.001). Higher than 1 M KCl, there may be interesting mass accommodation phenomena occurring at the interface as the aqueous solution approaches a saturated solution (at ~4.5 M) and crystallization begins to occur. Further work must be performed to determine the nature of the AC coefficient when the molality is greater than 1 for KCl.

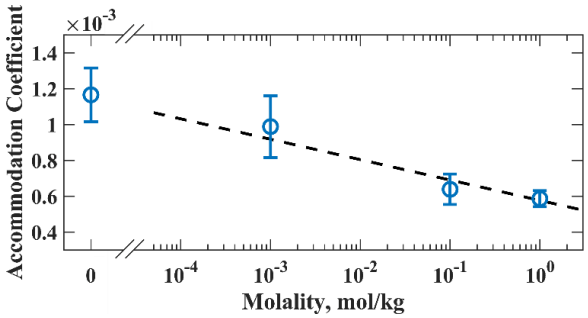

Figure 6 Mean AC and associated uncertainty over the first 120 seconds of evaporation for four droplets of varying KCl concentration. The dotted black line is for visualization of a trend in variation of the accommodation coefficient

CONCLUSION

Evaporation is a complex, highly-coupled heat and mass transfer phenomenon essential in nature and many industrial applications. The fundamental understanding of factors that influence evaporation is critical to device and system design towards solving challenging problems such as electronics cooling and water desalination. This study performs a coupled experimental-computational investigation of aqueous saline droplets of KCl evaporating into a dry nitrogen stream. This work couples experiments using a QCM to serve as a precise instantaneous radius sensor with a multiscale computational analysis considering the Knudsen layer and the macroscale heat transfer and gas flow around the droplet. This analysis allowed for the determination of the accommodation coefficient in Schrage's binary gas equations (Eq. (1)) for water with a non-condensable gas (nitrogen).

This work finds the surface-averaged accommodation coefficient to decrease with increasing KCl concentration reaching a value of $5.86 \times 10^{-4} \pm 0.45 \times 10^{-4}$ for an initial concentration of 1 M KCl. This value is approximately a factor of two below the accommodation coefficient of the 0 M KCl or pure water droplet ($11.7 \times 10^{-4} \pm 1.5 \times 10^{-4}$). While both values are low compared to a theoretical value of unity for a pure water droplet, significant impurities and non-condensable gas are present in both cases. Specifically, the molar fraction of nitrogen gas near the interface is ~0.97 for all droplets, and the saline droplets have KCl concentrations approaching a saturated solution. Since these conditions are common in real-world applications, we believe this study provides a basis for predicting evaporative flux at the liquid-vapour interface and the device performance when non-condensable gases and non-volatile impurities are intrinsic to the application.

REFERENCES

[1] A.M. Cazabat, G. Guéna, Evaporation of macroscopic sessile droplets, Soft Matter. 6 (2010) 2591–2612.

[2] S. David, K. Sefiane, L. Tadrist, Experimental investigation of the effect of thermal properties of the substrate in the wetting and evaporation of sessile drops, Colloids Surfaces A Physicochem. Eng. Asp. 298 (2007) 108–114.

[3] W.L. Cheng, W.W. Zhang, H. Chen, L. Hu, Spray cooling and flash evaporation cooling: The current development and application, Renew. Sustain. Energy Rev. 55 (2016) 614–628.

[4] V. Soulié, F. Lequien, F. Ferreira-Gomes, G. Moine, D. Feron, P. Prene, H. Moehwald, T. Zemb, H. Riegler, Salt-induced iron corrosion under evaporating sessile droplets of aqueous sodium chloride solutions, Mater. Corros. 68 (2017) 927–934.

[5] H.T. El-Dessouky, H.M. Ettouney, Multiple-effect evaporation desalination systems: Thermal analysis, Desalination. 125 (1999) 259–276.

[6] S.Y. Misyura, Evaporation of a sessile water drop and a drop of aqueous salt solution, Sci. Rep. 7 (2017).

[7] S.Y. Misyura, Evaporation and heat transfer of aqueous salt solutions during crystallization, Appl. Therm. Eng. 139 (2018) 203–212.

[8] R.W. Schrage, A Theoretical Study of Interphase Mass Transfer, Columbia University Press, New York, 1953.

[9] R. Marek, J. Straub, Analysis of the evaporation coefficient and the condensation coefficient of water, Int. J. Heat Mass Transf. 44 (2001) 39–53.

[10] P. Jafari, A. Amritkar, H. Ghasemi, Temperature Discontinuity at an Evaporating Water Interface, J. Phys. Chem. C. 124 (2020) 1554–1559.

[11] G. Sauerbrey, Verwendung von Schwingquarzen zur Wägung dünner Schichten und zur Mikrowägung, Zeitschrift Für Phys. 155 (1959) 206–222.

[12] B. Murray, S. Narayanan, The Role of Wettability on the Response of a Quartz Crystal Microbalance Loaded with a Sessile Droplet, Sci. Rep. 9 (2019) 1–13.

[13] B. Murray, M.J. Fox, S. Narayanan, Quantifying the evaporation rate of sessile droplets using a quartz crystal microbalance, J. Appl. Phys. 128 (2020) 035101.

[14] D. York, N.M. Evensen, M.L. Martínez, J. De Basabe Delgado, Unified equations for the slope, intercept, and standard errors of the best straight line, Am. J. Phys. 72 (2004) 367–375.

[15] S. COMSOL AB, COMSOL Multiphysics ® v. 5.5, (2019).

[16] F. Girard, M. Antoni, K. Sefiane, On the effect of Marangoni flow on evaporation rates of heated water drops, Langmuir. 24 (2008) 9207–9210.

[17] A.A. Zavitsas, Quest to Demystify Water: Ideal Solution Behaviors Are Obtained by Adhering to the Equilibrium Mass Action Law, J. Phys. Chem. B. 123 (2019) 869–883.

[18] J.R. ed. Rumble, Handbook of Chemistry and Physics 100th Edition, 100th ed., CRC Press, Boca Raton, FL, 2019.

[19] R.A. Robie, B.S. Hemingway, Thermodynamic Properties of Minerals and Related Substances at 298.15K and 1 Bar (105 Pascals) Pressure and at Higher Temperatures, 1995.

[20] M.L.V. Ramires, C.A. Nieto De Castro, Thermal conductivity of aqueous potassium chloride solutions, Int. J. Thermophys. 21 (2000) 671–679.

[21] I.D. Zaytsev, G.G. Aseyev, Properties of Aqueous Solutions of Electrolytes, CRC Press, Boca Raton, FL, 1992.